General Method to Foresee the Behavior of Virtual Synchronous Machines working with Distorted and Unbalanced Voltage Conditions

General Method to Foresee the Behavior of Virtual Synchronous Machines working with Distorted and Unbalanced Voltage Conditions

Vincenzo Mallemaci, *Student Member, IEEE*, Fabio Mandrile, *Member, IEEE*, Enrico Carpaneto, *Member, IEEE*, and Radu Bojoi, *Fellow, IEEE*

***Abstract*—To make photovoltaic and wind power plants able to provide grid services (i.e., inertial behavior, grid support and harmonic compensation), several control algorithms have been proposed in the literature during the last years. The most promising ones make the power electronic converters behave as conventional alternators, using the concept of Virtual Synchronous Machine (VSM). Several VSM models are available in the literature, some of which can improve the voltage quality at the point of connection with the grid behaving as harmonic and unbalance sinks under non–ideal grid voltage conditions. However, the literature lacks a general method to foresee the behavior of a generic VSM configuration in such conditions along with a well–established definition of the needed features to make VSMs able to work as harmonic or unbalance sinks. Therefore, this paper proposes a simple and general method to foresee the behavior of different VSM configurations under non–ideal grid voltage conditions before any experimental verification. The proposed method accurately foresees the VSMs behavior, as experimentally demonstrated on five VSM models available in the literature, working with fifth harmonic and inverse sequence voltage distortions. Moreover, the method identifies which VSM configuration can feature a beneficial harmonic and unbalance compensation.**

***Index Terms*—Harmonic Sink, Renewable Energy Sources (RESs), Virtual Synchronous Machine (VSM).**

I. Introduction

In the next years, renewable power plants (especially solar and wind) are expected to provide grid services as normally performed by thermoelectric and hydroelectric power plants. The inertial behavior and the support of the grid during faults are two main examples [1]. The employment of power electronic converters is essential to connect renewable energy sources to the electric grid, but their conventional control techniques are not suitable to provide the aforementioned grid services. Therefore, during the last 15 years, many different solutions have been proposed to overcome this issue. Some of the proposed solutions are based on the concept of Virtual Synchronous Machine (VSM) [2]–[4]. According to this approach, power electronic converters can behave as conventional synchronous machines (SMs) by providing the aforementioned grid services. Moreover, they can show superior performance to SMs, even in the case of non–ideal grid voltage conditions [5].

The literature reports some VSM implementations that can improve the voltage quality at the point of connection with the grid through harmonic current flow, behaving as sinks for harmonics and unbalances [6]–[10]. As example, [6] proposes a control with parallel virtual admittances, tuned at specific harmonics to compensate for the voltage distortion at the point of connection with the grid. An impedance–based harmonic current distortion suppression method is proposed in [7] and compared with other two conventional methods. Paper [8] evaluates the performance of five different strategies for controlling the negative sequence current for the operation of a VSM model under unbalanced conditions. In [9] a hybrid harmonic suppression scheme is integrated into a VSM algorithm. The scheme consists of a local voltage harmonic control loop and an adaptive grid current–controlled loop, with a concurrent distortion inhibition capability. Finally, [10] identifies the pros and cons of different control strategies that combine VSM and active filter capabilities.

In general, the papers dealing with VSM behavior with non–ideal grid voltage operating conditions focus on a specific VSM implementation. As a result, a simple general method to foresee the behavior of a generic VSM configuration under non–ideal grid voltage conditions along with a well–established definition of the needed features to make a VSM able to work as a harmonic or unbalance sink, are not available in the literature.

Therefore, the paper proposes a methodology with high degree of generality that allows to foresee the VSM models response from the point of view of the power quality, i.e., the behavior of VSMs under distorted and unbalanced grid voltage conditions. Although the literature includes many VSM solutions, according to our best knowledge the literature lacks a paper showing that VSMs can or not provide such service according to their category (current or voltage source) and the type of virtual impedance implementation (complete, simplified, or not implemented). This work aims at filling this gap, by providing a simple and general method to foresee the behavior of different VSM configurations under non–ideal grid voltage conditions before any experimental verification. Moreover, this paper assesses the needed features to make a

The authors acknowledge the support of the Power Electronics Innovation Center (PEIC) of the Politecnico di Torino. V. Mallemaci, F. Mandrile, E. Carpaneto and R. Bojoi are with the Dipartimento Energia ”G. Ferraris”, Politecnico di Torino, Torino, 10129, Italy (e-mail: vincenzo.mallemaci@polito.it).

VSM able to behave as harmonic and unbalance sinks, by identifying which VSM configuration can feature a beneficial harmonic and unbalance compensation by improving the voltage quality at the point of common coupling (PCC).

The proposed method has been applied to five VSM models available in the literature. The five VSM models considered in this paper are: Simplified Virtual Synchronous Compensator (S–VSC) [11], Virtual Synchronous Machine (VISMA) II [12], Osaka [13], [14], the enhanced version of the Osaka model (hereinafter called Osaka II) [15] and Kawasaki Heavy Industries (KHI) [16], [17]. Each of them belongs to a different VSM configuration, which will be described in the following section. Moreover, other two VSM models have been implemented and tested to compare their behavior with the aforementioned five VSMs: VISMA [18], [19] and VSYNC [20].

The considered VSM models have been implemented on a standard grid–tied inverter, as described in Fig. 1. The VSM Model block contains the implemented VSM algorithms. It provides the voltage reference given to the PWM modulator. The complete control diagrams of the implemented VSMs can be found in [4], as well as in their corresponding papers [11]–[14], [16]–[20]. All the VSM models have the same design parameters (e.g., virtual stator inductance and resistance, virtual inertia, damping coefficient, etc.) to provide a fair comparison [4]. The main data of the setup are listed in Table I, together with the VSM parameters. Base values have been defined to express most of the parameters in per unit. The experimental validation has been performed for the following testing conditions related to the grid voltage e_g:

- Test 1: 5% of fifth harmonic, the most dominant non–fundamental component in non–ideal three phase systems;
- Test 2: 5% of inverse sequence distortion, which occurs in case of asymmetrical faults.

The chosen testing conditions represent the most likely grid voltage non–idealities and they are significant to highlight the differences among the implemented VSM configurations.

For the above mentioned testing conditions, the expected beneficial effects of VSMs are, respectively, a reduction of the fifth harmonic distortion and a decrease of the voltage unbalance factor (VUF) on the PCC voltage v_c. These represent the needed requirements to establish if a VSM behaves as, respectively, harmonic and unbalance sink.

This paper is organized as follows. Section II provides a general overview of VSMs. In Section III the simplified modeling approach is described and the theoretical results are retrieved. Section IV shows the experimental results of the aforementioned tests. Finally, the conclusions are given in Section V.

II. VSM Models

The virtual stator of the VSM can be modeled as an equivalent Thévenin circuit consisted of a virtual electromotive force generator e_v and a virtual impedance Z_v, including a virtual resistance R_v and a virtual inductance L_v.

The VSMs can be gathered in two main categories: current source VSMs and voltage source VSMs [4]. The former

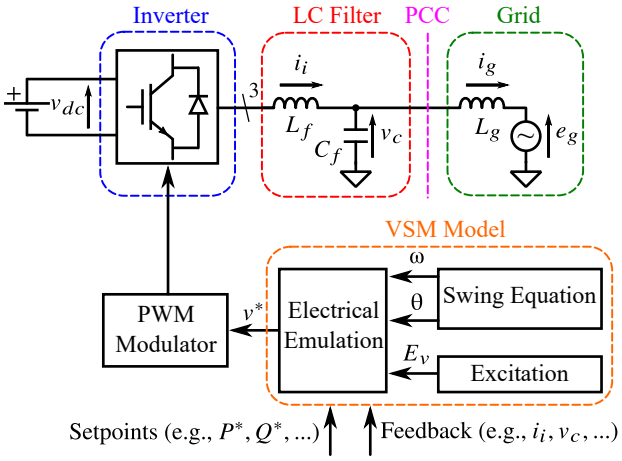

Fig. 1: Considered hardware for VSM implementations.

TABLE I: System parameters.

Inverter		Base Values			
S_N	15 kVA	S_b	15 kVA	f_b	50 Hz
I_N	30 A	V_b	$230\sqrt{2}$ V	ω_b	314 rad/s
f_{sw}	10 kHz	I_b	30 A	L_b	33.7 mH
V_{dc}	650 V	Z_b	10.6 Ω	C_b	0.3 mF
Virtual Impedance		**LC Filter**		**Grid**	
R_v	0.02 pu	R_f	0.024 pu	$\widehat{E}_g$	$230\sqrt{2}$ V
L_v	0.15 pu	L_f	0.059 pu	R_g	0.007 pu
		C_f	0.017 pu	L_g	0.009 pu

provides the current reference i_i^* to a current regulator to obtain the duty cycles for the inverter switches. The latter directly calculates the voltage reference v^* with no regulators.

Current source VSMs employ a tunable virtual impedance Z_v to create the current reference from the difference between the virtual electromotive force e_v and the PCC voltage v_c, as follows:

$$i_i^* = \frac{e_v - v_c}{Z_v} \tag{1}$$

The connection between the current source VSM and the electric grid can be modeled with the single phase equivalent circuit in Fig. 2a, where L_g is the grid inductance, R_g is the grid resistance and C_f is the LC filter capacitance.

On the contrary, voltage source VSMs create the voltage reference by subtracting the voltage drop on the tunable virtual impedance Z_v to the virtual electromotive force e_v, as shown in (2).

$$v^* = e_v - Z_v i_i \tag{2}$$

The grid connection can be modeled with the single phase equivalent circuit depicted in Fig. 2b. Here, L_f is the filter inductance and R_f is the filter resistance. The other elements are the same of Fig. 2a.

III. Theoretical Analysis

In the (d, q) reference frame rotating at the fundamental frequency ω, the generic quantity $\bar{x}$ can be written as follows:

$$\bar{x} = x_d + jx_q \tag{3}$$

where j is the imaginary unit, while x_d and x_q are the two components of $\bar{x}$ on the d–axis and the q–axis, respectively.

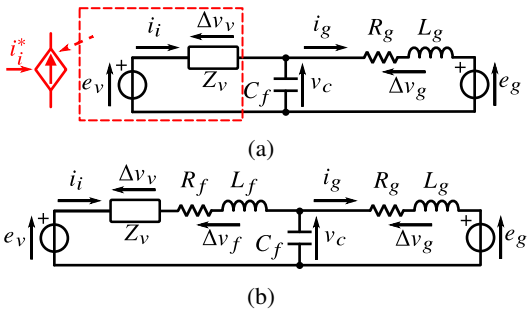

Fig. 2: Equivalent circuits of connection between the grid and the inverter: (a) current source models; (b) voltage source models.

Considering the equivalent circuits of Fig. 2, the capacitor current can be assumed negligible for the purpose of this paper as it is much lower than the inverter current. Therefore, the grid current i_g can be considered equal to the inverter current i_i. With this approximation, the Kirchhoff's voltage law for the circuit in Fig. 2a in the (d,q) reference frame rotating at ω, is the following:

$$\begin{aligned}\bar{e}_v &= R_v\bar{i}_i + L_v\frac{d\bar{i}_i}{dt} + j\omega L_v\bar{i}_i + \bar{v}_c\\ \bar{e}_v &= \Delta\bar{v}_v + \bar{v}_c\\ &= \Delta\bar{v}_v + R_g\bar{i}_i + L_g\frac{d\bar{i}_i}{dt} + j\omega L_g\bar{i}_i + \bar{e}_g\\ &= \Delta\bar{v}_v + \Delta\bar{v}_g + \bar{e}_g\end{aligned} \tag{4}$$

For the generic harmonic order h, the derivative term at steady state is:

$$\frac{d}{dt} \rightarrow jh\omega \tag{5}$$

Consequently, (4) is evaluated for the h–th order:

$$\begin{aligned}\bar{e}_v^h &= \Delta\bar{v}_v^h + \bar{v}_c^h\\ &= \Delta\bar{v}_v^h + R_g\bar{i}_i^h + j(h+1)\omega L_g\bar{i}_i^h + \bar{e}_g^h\\ &= \Delta\bar{v}_v^h + \Delta\bar{v}_g^h + \bar{e}_g^h\end{aligned} \tag{6}$$

The same applies to the equivalent circuit in Fig. 2b:

$$\bar{e}_v = \Delta\bar{v}_v + \Delta\bar{v}_f + \Delta\bar{v}_g + \bar{e}_g \tag{7}$$

$$\bar{e}_v^h = \Delta\bar{v}_v^h + \Delta\bar{v}_f^h + \Delta\bar{v}_g^h + \bar{e}_g^h \tag{8}$$

The virtual impedance Z_v can be considered as:

- Complete virtual impedance (CVI). No simplifications are performed on the Kirchhoff's voltage law (4) since the virtual impedance behaves like a real impedance.
- Simplified virtual impedance (SVI). The derivative term in (4) is neglected and the reactance is the same for each harmonic component. In this case, the virtual impedance does not behave like a real one.
- Not implemented (NI). The virtual impedance is not implemented.

Six VSM configurations can be been identified according to their category (current or voltage source) and how the virtual impedance is implemented. These configurations are listed below:

A. *Current source with CVI*. The analysis and the results are carried out for the S–VSC model, but they can be extended for other current source VSMs available in the literature, such as VISMA I [21], Synchronverter [22] and Synchronous Power Controller (SPC) [23]–[25]. Moreover, the same analysis can be applied to [26]–[29].

B. *Voltage source with CVI*. The VSM model under analysis is the VISMA II.

C. *Current source with SVI*. The KHI model is the VSM implemented to analyze this kind of configuration. The simplified modeling and the results are also valid for the Cascaded Virtual Synchronous Machine (CVSM) [30], [31]. The same approach can be extended to other VSM available in the literature [32], [33].

D. *Voltage source with NI*. The considered VSM model for the modeling validation is the Osaka model. The results are also valid for other grid–forming VSMs with no virtual impedance, such as [34], [35].

E. *Voltage source with SVI*. The VSM model chosen for the modeling validation is the Osaka II model.

F. *Current source with NI*. This last configuration gathers two current source models which do not embed a virtual impedance: VISMA and VSYNC. No simplified models have been retrieved for them, but they have been implemented and tested to compare their responses with the five previous configurations.

A. Current source with CVI

Starting from (4), the equivalent circuit of current source with CVI VSMs is shown in Fig. 3a. For the h–th harmonic order, (4) becomes:

$$\begin{aligned}\bar{e}_v^h &= R_v\bar{i}_i^h + jh\omega L_v\bar{i}_i^h + j\omega L_v\bar{i}_i^h + \bar{v}_c^h\\ &= \underbrace{(R_v + R_g)}_{R_{eq}}\bar{i}_i^h + j\underbrace{(h+1)\omega(L_v + L_g)}_{X_{eq}^h}\bar{i}_i^h + \bar{e}_g^h\\ &= (R_{eq} + jX_{eq}^h)\bar{i}_i^h + \bar{e}_g^h\end{aligned} \tag{9}$$

This method can be also applied to the VSM proposed in [26], where the virtual impedance shows a virtual capacitor which can be included in the equivalent reactance X_{eq}^h. Moreover, (9) is valid even for VSMs which employ a complete and adaptive virtual impedance, where the amplitudes of the virtual resistance and inductance can change according to their control algorithm [27], [28]. Finally, [29] uses a complete virtual impedance with a low–pass filter. In this case, the harmonic and unbalance sink capabilities depend on the cut–off frequency of the filter. Eq. (9) can be used by including the low–pass filter on the virtual impedance.

B. Voltage source with CVI

This configuration refers to the equivalent circuit of Fig. 2b. The Kirchhoff's voltage laws (7) and (8) become respectively (10) and (11):

$$\bar{e}_v = (R_v + R_f)\bar{i}_i + (L_v + L_f)\frac{d\bar{i}_i}{dt} + j\omega(L_v + L_f)\bar{i}_i + \bar{v}_c \tag{10}$$

$$\begin{aligned}\bar{e}_v^h =&(R_v + R_f)\bar{i}_i^h + j(h+1)\omega(L_v + L_f)\bar{i}_i^h + \bar{v}_c^h \\ =&\underbrace{(R_v + R_f + R_g)}_{R_{eq}}\bar{i}_i^h + \\ &+ j\underbrace{(h+1)\omega(L_v + L_f + L_g)}_{X_{eq}^h}\bar{i}_i^h + \bar{e}_g^h \\ =&(R_{eq} + jX_{eq}^h)\bar{i}_i^h + \bar{e}_g^h\end{aligned} \tag{11}$$

The equivalent circuit is shown in Fig. 3b.

In conclusion, it can be observed that for the VSM configurations with a complete virtual impedance (i.e., A and B configurations), the virtual reactance behaves like the real ones (i.e., filter and grid reactances). The reactance is directly proportional to the harmonic order and the voltage drop on the virtual impedance Δv_v^h contributes with the same sign of the voltage drop on the grid impedance Δv_g^h, independently of the harmonic order. Moreover, the configuration B shows the additional contribution of the filter impedance Z_f with a consequent larger equivalent impedance.

C. Current source with SVI

This configuration shows a simplified implementation of the virtual impedance, where the derivative term is zero. (4) becomes:

$$\begin{aligned}\bar{e}_v &= R_v\bar{i}_i + L_v\cancel{\frac{d\bar{i}_i}{dt}} + j\omega L_v\bar{i}_i + \bar{v}_c \\ &= R_v\bar{i}_i + j\omega L_v\bar{i}_i + \bar{v}_c\end{aligned} \tag{12}$$

The equivalent circuit in the (d,q) reference frame is depicted in Fig. 3c. For the h–th harmonic order, (12) becomes:

$$\begin{aligned}\bar{e}_v^h &= R_v\bar{i}_i^h + j\omega L_v\bar{i}_i^h + \bar{v}_c^h \\ &= \underbrace{(R_v + R_g)}_{R_{eq}}\bar{i}_i^h + j\underbrace{\omega\left[L_v + (h+1)L_g\right]}_{X_{eq}^h}\bar{i}_i^h + \bar{e}_g^h \\ &= (R_{eq} + jX_{eq}^h)\bar{i}_i^h + \bar{e}_g^h\end{aligned} \tag{13}$$

From (13), it can be noted that the virtual impedance is independent of the harmonic order. It behaves like a real impedance only for the fundamental frequency (i.e., $h = 0$). Indeed, for $h \neq 0$, the equivalent reactance is expected to be lower than the X_{eq}^h of configurations A and B. This implies higher current circulation under the same operating conditions. Moreover, for $h < 0$ (e.g., inverse sequence, 5^{th} harmonic, 11^{th} harmonic, etc.), $|X_{eq}^h|$ is:

$$|X_{eq}^h| = |\omega L_v - (|h| - 1)\omega L_g| \tag{14}$$

It is evident from (14) that the virtual and grid reactances contribute with opposite signs if $h < 0$. Finally, in the case of $\omega L_v = (|h| - 1)\omega L_g$, the equivalent reactance is zero and the current is limited only by the equivalent resistance, with the risk of overcurrent faults.

The same approach can be also applied to the VSM proposed in [33]. As in [29], a low–pass filter is used with the virtual impedance. As stated before, the harmonic and unbalance sink capabilities are influenced by the cut–off frequency of the filter. Moreover, the amplitudes of the virtual resistance and reactance are adaptive according to the working condition. Nevertheless, (13) is still valid.

D. Voltage source with NI

The connection of the configuration D with the grid can be modeled with the same circuit of Fig. 2b by considering a zero virtual impedance. Indeed, according to this configuration, the electromotive force is directly used as the voltage reference for the inverter. For the purpose of this paper, the arbitrary limitation resistance used in [13] is set to zero. The Kirchhoff's voltage law becomes:

$$\bar{e}_v = R_f\bar{i}_i + L_f\frac{d\bar{i}_i}{dt} + j\omega L_f\bar{i}_i + \bar{v}_c \tag{15}$$

The equivalent circuit in the (d,q) reference frame is shown in Fig. 3d. For the h–th harmonic order, (15) is:

$$\begin{aligned}\bar{e}_v^h &= R_f\bar{i}_i^h + jh\omega L_f\bar{i}_i^h + j\omega L_f\bar{i}_i^h + \bar{v}_c^h \\ &= \underbrace{(R_f + R_g)}_{R_{eq}}\bar{i}_i^h + j\underbrace{(h+1)\omega(L_f + L_g)}_{X_{eq}^h}\bar{i}_i^h + \bar{e}_g^h \\ &= (R_{eq} + jX_{eq}^h)\bar{i}_i^h + \bar{e}_g^h\end{aligned} \tag{16}$$

It can be observed that for this configuration the behavior under non–ideal grid voltage conditions is strictly dependent on the physical parameters of the system, with no possibilities to tune the equivalent impedance, as it happens for configurations A, B and C.

E. Voltage source with SVI

The same methodology used in III-C can be used for voltage source VSMs with SVI. Starting from the equivalent circuit in Fig. 2b, (10) and (11) become respectively (17) and (18):

$$\bar{e}_v = (R_v + R_f)\bar{i}_i + L_f\frac{d\bar{i}_i}{dt} + j\omega(L_v + L_f)\bar{i}_i + \bar{v}_c \tag{17}$$

$$\begin{aligned}\bar{e}_v^h =&(R_v + R_f)\bar{i}_i^h + j\omega\left[L_v + (h+1)L_f\right]\bar{i}_i^h + \bar{v}_c^h \\ =&\underbrace{(R_v + R_f + R_g)}_{R_{eq}}\bar{i}_i^h + \\ &+ j\underbrace{\omega\left[L_v + (h+1)(L_f + L_g)\right]}_{X_{eq}^h}\bar{i}_i^h + \bar{e}_g^h \\ =&(R_{eq} + jX_{eq}^h)\bar{i}_i^h + \bar{e}_g^h\end{aligned} \tag{18}$$

The equivalent circuit in the (d,q) reference frame is shown in Fig. 3e.

Considering $h < 0$ (e.g., inverse sequence, 5^{th} harmonic, 11^{th} harmonic, etc.), $|X_{eq}^h|$ is:

$$|X_{eq}^h| = |\omega L_v - (|h| - 1)\omega(L_f + L_g)| \tag{19}$$

As it happens for current source VSMs with SVI, even for this configuration the virtual and physical reactances contribute

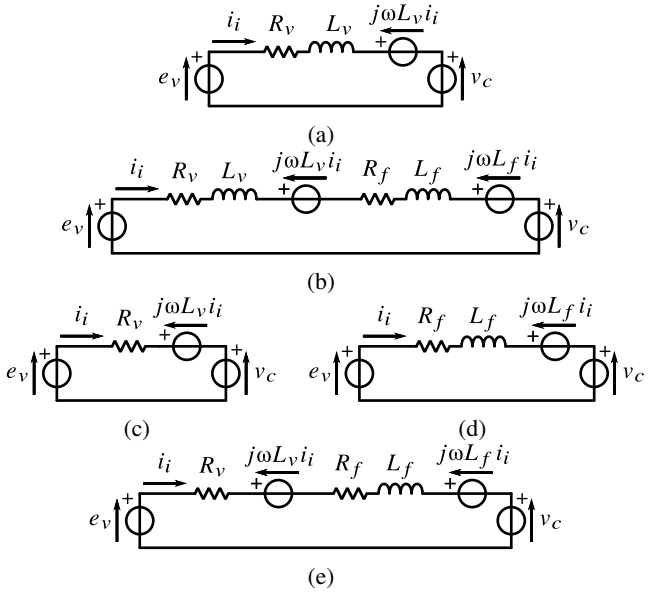

Fig. 3: Equivalent circuits in the (d, q) rotating reference frame for configurations: (a) A; (b) B; (c) C; (d) D; (e) E.

with opposite signs if $h < 0$. In the case of $\omega L_v = (|h| - 1)\omega(L_f + L_g)$, the equivalent reactance is zero and the current is limited only by the equivalent resistance, with the risk of overcurrent faults.

F. Current source with NI

This final group is dedicated to two current source models which do not embed a virtual impedance.

VISMA is a VSM model based on the 7^{th} order electromagnetic model of conventional synchronous generators. Therefore, the choice of its parameters and the behavior analysis refers to [36], [37].

Finally, the VSYNC is a peculiar VSM model based on the Phase Locked Loop (PLL) working principle. It does not embed a virtual stator implementation. Indeed, it produces the current references from the active power retrieved by the PLL structure and the external reactive power reference [20]. Therefore, its behavior under distorted grid voltage conditions is strictly dependent on the PLL performance [38].

G. Theoretical Conclusions

In the (d, q) reference frame, synchronous with the fundamental frequency of 50 Hz ($h = 0$), the fifth harmonic and the inverse sequence correspond to 300 Hz ($h = -6$) and 100 Hz ($h = -2$), respectively. The virtual electromotive force e_v, produced by the VSM, is zero for each $h \neq 0$. Consequently, the current amplitude $|\bar{i}_i^h|$ can be easily retrieved as follows:

$$|\bar{i}_i^h| \approx |\bar{i}_g^h| = \frac{|\bar{e}_g^h|}{\sqrt{R_{eq}^2 + X_{eq}^{h,2}}} \tag{20}$$

where the grid voltage amplitude $|\bar{e}_g^h|$ is 5% both with $h = -6$ and with $h = -2$.

Finally, the PCC voltage amplitude $|\bar{v}_c^h|$ can be computed from the voltage divider equation:

$$|\bar{v}_c^h| = \sqrt{\frac{R_i^2 + X_i^{h,2}}{R_{eq}^2 + X_{eq}^{h,2}}}\,|\bar{e}_g^h| \tag{21}$$

where R_i and X_i^h are, respectively, the equivalent resistance and reactance on the inverter side (i.e., between e_v and v_c) for the harmonic h.

From (21), a VSM improves the voltage quality at the PCC if:

$$\sqrt{\frac{R_i^2 + X_i^{h,2}}{R_{eq}^2 + X_{eq}^{h,2}}} < 1 \iff (R_i R_g + X_i^h X_g^h) > -\frac{R_g^2 + X_g^{h,2}}{2} \tag{22}$$

Assuming positive values for R_v and L_v, configurations A, B and D always satisfies (22) because the term $(R_i R_g + X_i^h X_g^h)$ is always positive. Therefore, they are expected to reduce both the fifth harmonic distortion and the unbalance of the PCC voltage independently on the virtual impedance parameters. On the opposite, for the configurations C and E the term $(R_i R_g + X_i^h X_g^h)$ can be negative, because their virtual and physical reactances contribute with opposite signs.

For the configurations C and E, (22) can be written respectively as (23) and (24):

$$(R_v R_g + \omega L_v X_g^h) > -\frac{R_g^2 + X_g^{h,2}}{2} \tag{23}$$

$$[(R_v + R_f)R_g + (\omega L_v + X_f^h)X_g^h] > -\frac{R_g^2 + X_g^{h,2}}{2} \tag{24}$$

According to the values listed in Table I, the configuration C amplifies the voltage distortions because (23) is never satisfied, whereas configuration E reduces the fifth harmonic distortion but amplifies the unbalance of the PCC voltage because (24) is satisfied only for the fifth harmonic distortion. More in general, (22) allows quantifying the beneficial or negative effect of the VSM under study. The results of the theoretical analysis are collected in Table II and Fig. 4.

Moreover, it is also possible to apply this method separately for the d–axis and q–axis, for instance in case of asymmetric impedances on the two axes.

In conclusion, the stability of the configurations A, B, C, D and E is discussed in Appendix A.

IV. Experimental Tests

Two experimental tests have been carried out to validate the simplified method:

- Test 1: grid voltage e_g with 5% of fifth harmonic. In three phase systems, the fifth harmonic is typically generated by non–linear loads and it is the most dominant non–fundamental harmonic component. When the VSM control is disabled, the Discrete Fourier Transform (DFT) of the PCC line to line voltage $v_{c,ll}$ measures about 28 V on the fifth harmonic;
- Test 2: grid voltage e_g with 5% of inverse sequence. The grid voltage can contain inverse sequence, for instance, in case of asymmetrical faults. The VUF, defined in the standard EN 50160, is calculated for the PCC line to line voltage $v_{c,ll}$ to quantify the inverse sequence contribution.

TABLE II: Results of the theoretical analysis.

Configuration	Model	R_{eq}	X^h_{eq}		
			Harmonic h	5^{th} Harmonic ($h=-6$)	Inverse Sequence ($h=-2$)
A: Current source with CVI	S–VSC	R_v+R_g	$(h+1)\omega(L_v+L_g)$	$-5\omega(L_v+L_g)$	$-\omega(L_v+L_g)$
B: Voltage source with CVI	VISMA II	$R_v+R_f+R_g$	$(h+1)\omega(L_v+L_f+L_g)$	$-5\omega(L_v+L_f+L_g)$	$-\omega(L_v+L_f+L_g)$
C: Current source with SVI	KHI	R_v+R_g	$\omega L_v+(h+1)\omega L_g$	$\omega(L_v-5L_g)$	$\omega(L_v-L_g)$
D: Voltage source with NI	Osaka	R_f+R_g	$(h+1)\omega(L_f+L_g)$	$-5\omega(L_f+L_g)$	$-\omega(L_f+L_g)$
E: Voltage source with SVI	Osaka II	$R_v+R_f+R_g$	$\omega L_v+(h+1)\omega(L_f+L_g)$	$\omega[L_v-5(L_f+L_g)]$	$\omega[L_v-(L_f+L_g)]$

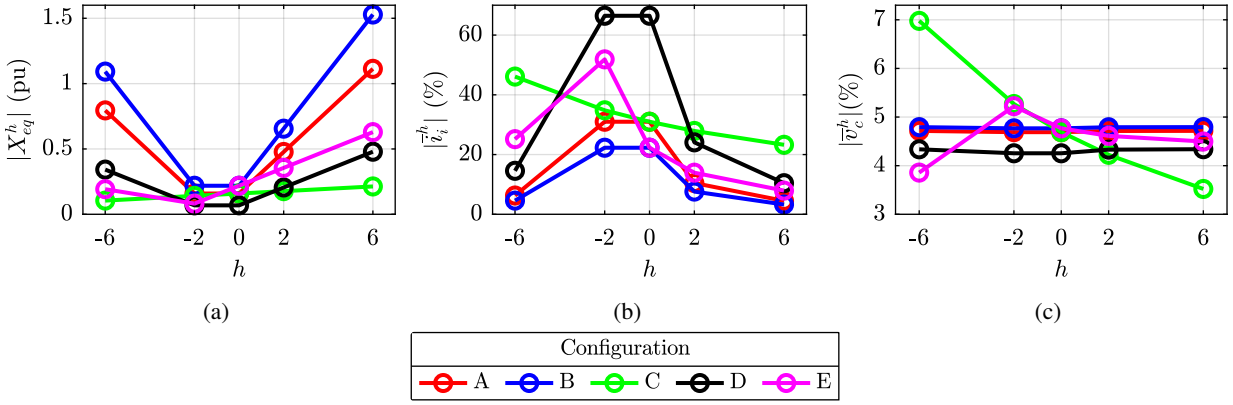

Fig. 4: Theoretical values of: (a) equivalent reactance $|X^h_{eq}|$; (b) current amplitude $|\bar{i}^h_i|$; (c) PCC voltage amplitude $|\bar{v}^h_c|$, where h is the harmonic order in the (d,q) rotating reference frame.

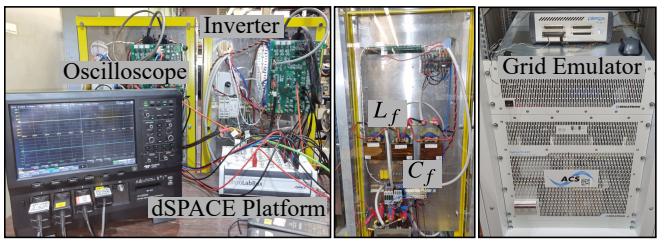

Fig. 5: Experimental setup.

When the VSM control is disabled, the PCC line to line voltage shows a VUF equal to 5%.

The values chosen for the tests are arbitrary and sufficient to appreciate the differences among the different configurations.

The setup used for the experimental validation is shown in Fig. 5. A two–level three phase inverter, controlled by a dSPACE platform, is connected to a grid emulator through an LC filter. The grid emulator imposes the three phase voltage e_g. The main data of the setup are listed in Table I.

A conventional PI regulator is employed for current source models. Moreover, two resonant current controllers are tuned for the second and sixth harmonic (i.e., respectively 100 Hz and 300 Hz) to make the inverter able to control the harmonic components.

A. Test 1: Fifth Harmonic

The results of Test 1 are evaluated by means of the DFT of the PCC line to line voltage $v_{c,ll}$ and the grid current i_g. They are shown in Fig. 6 and Fig. 7. The complete virtual impedance (i.e., S–VSC and VISMA II) enables harmonic compensation. The models which refer to configurations A and B behave as active filters, by improving the voltage quality at the PCC. Indeed, the fifth harmonic term decreases from 28 V to 26 V and 27 V, respectively for the S–VSC (Fig. 6a) and the VISMA II (Fig. 6b). Next, the Osaka model acts as a harmonic sink as well, even though it does not employ a virtual impedance (Fig. 6d). However, its effect is strictly dependent on the parameters of the physical connection to the grid (i.e., filter and grid impedances). In these three cases, the current drawn by the inverter produces a voltage drop on the grid impedance that reduces the harmonic distortion of the PCC voltage. The current waveforms together with their DFT are shown respectively in Fig. 7a, Fig. 7b and Fig. 7d. On the opposite, the KHI model amplifies the distortion, with an increment of the fifth harmonic to 39.7 V (Fig. 6c). The reason lies in the simplified structure of the virtual reactance. Indeed, as demonstrated in III-C and III-G, the voltage drops on the virtual and grid reactances have always opposite signs in the case of $h<0$ (i.e., 5^{th} harmonic and inverse sequence). As (22) is not satisfied, the PCC voltage distortion is amplified. The current waveform and its DFT are illustrated in Fig. 7c. Even the configuration E (i.e., Osaka II model) embeds a simplified structure of the virtual reactance as the configuration C. However, it satisfies (22). Therefore, it reduces the PCC voltage distortion as can be observed in Fig. 6e. The current waveform and its DFT are shown in Fig. 7e. Next, the VSYNC worsens the PCC voltage quality by increasing the fifth harmonic term and introducing a non–negligible seventh harmonic contribution as well (Fig. 6g and

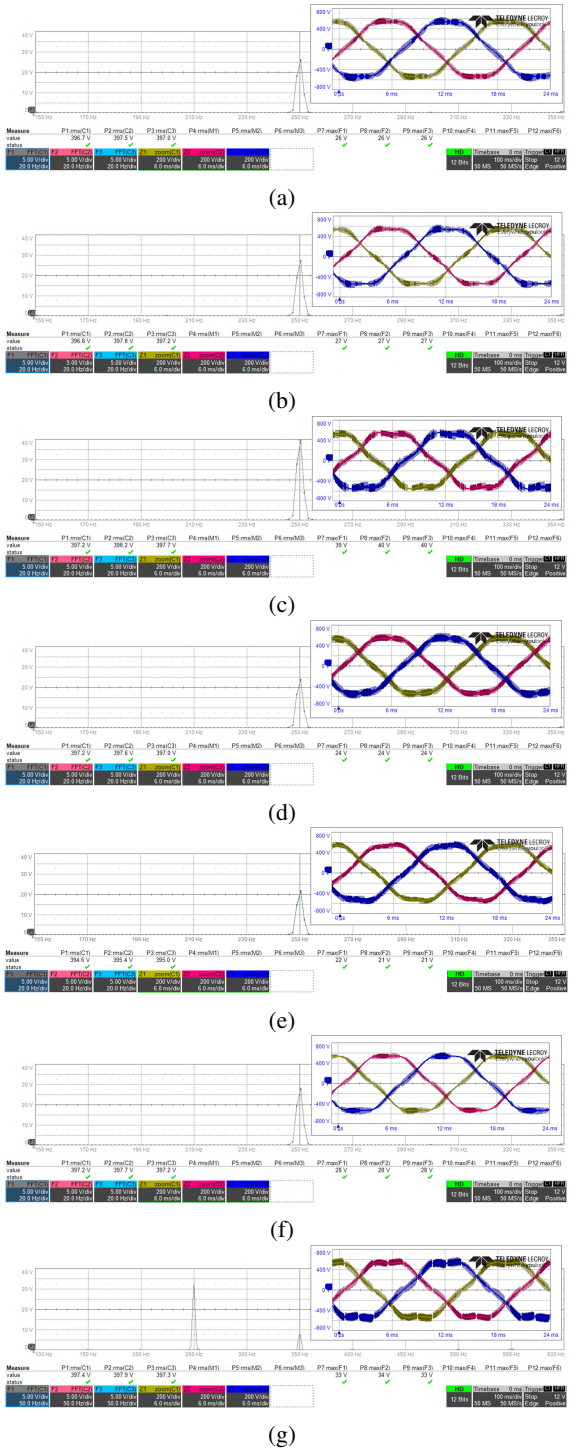

(a) (b) (c) (d) (e) (f) (g)

Fig. 6: Results of Test 1. DFT of the PCC line to line voltage $v_{c,ll}$, respectively for: (a) S–VSC; (b) VISMA II; (c) KHI; (d) Osaka; (e) Osaka II; (f) VISMA; (g) VSYNC.

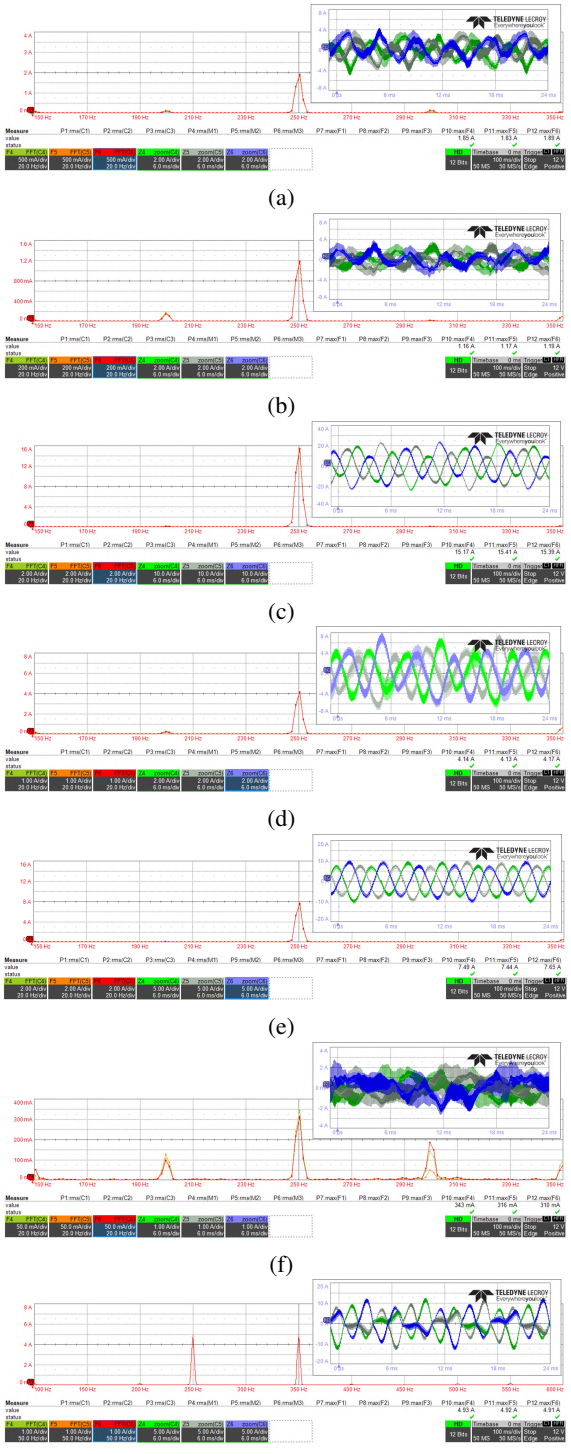

(a) (b) (c) (d) (e) (f) (g)

Fig. 7: Results of Test 1. DFT of the grid current i_g, respectively for: (a) S–VSC; (b) VISMA II; (c) KHI; (d) Osaka; (e) Osaka II; (f) VISMA; (g) VSYNC.

Fig. 7g). Finally, the VISMA model draws a negligible current which does not affect the PCC voltage (Fig. 7f). Indeed, the fifth harmonic term remains equal to 28 V (Fig. 6f). The results are summarized in Table III, where the theoretical results for VISMA and VSYNC come from PLECS simulations since no simplified models have been realized for these two VSMs.

B. Test 2: Inverse Sequence

The results of Test 2 are shown in Fig. 8 and summarized in Table IV. As in Table III, the theoretical results for VISMA and VSYNC come from PLECS simulations. Most of the comments for Test 1 are also valid for this second test. The S–

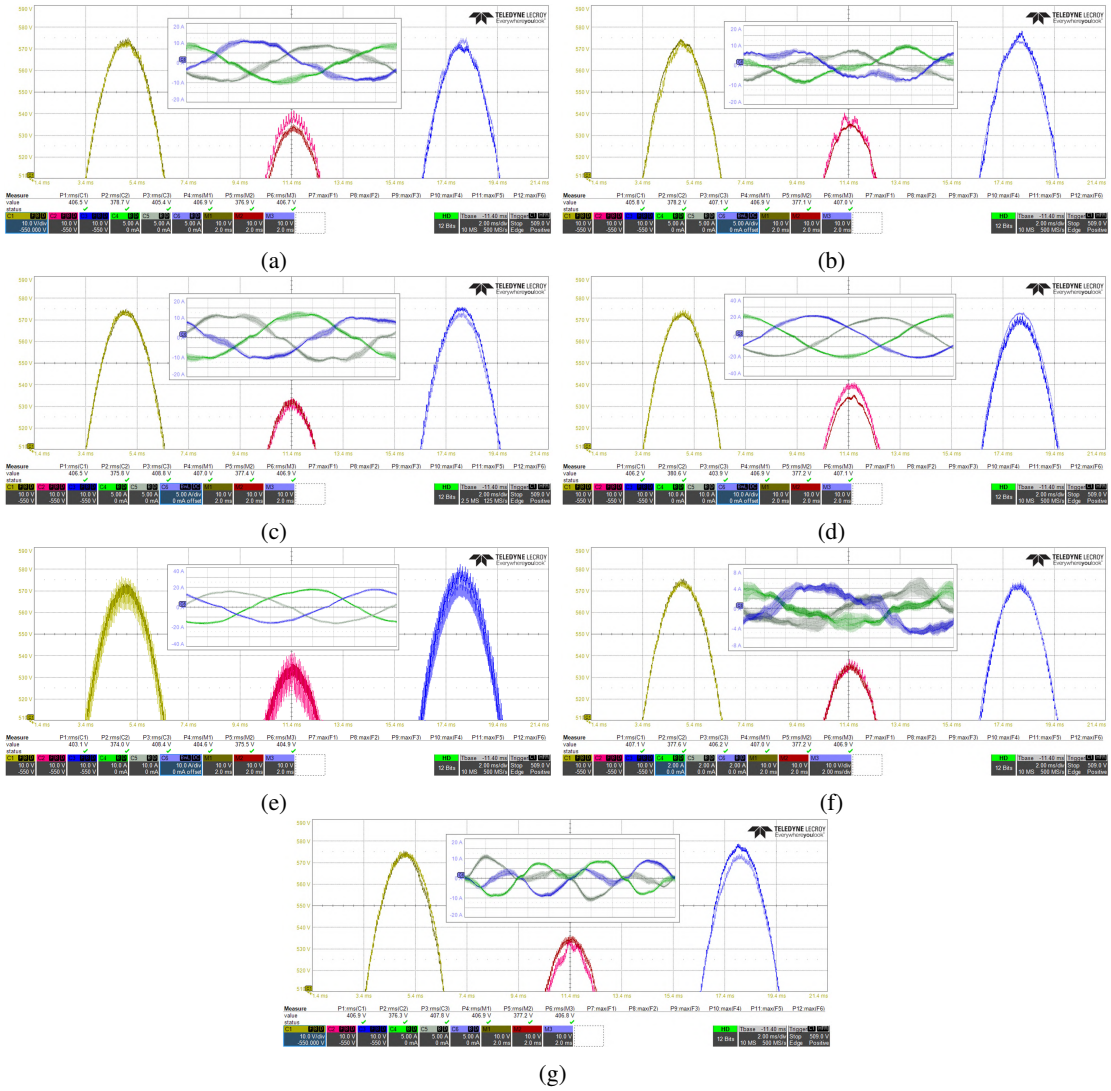

Fig. 8: Results of Test 2. M1, M2, M3: unbalanced PCC line to line voltage $v_{c,ll}$ without VSM control; C1, C2, C3: PCC line to line voltage $v_{c,ll}$ with VSM control; C4, C5, C6: grid current i_g with VSM control (time base: 2.0 ms/div). Models: (a) S–VSC; (b) VISMA II; (c) KHI; (d) Osaka; (e) Osaka II; (f) VISMA; (g) VSYNC.

TABLE III: Results of Test 1: Fifth Harmonic.

Model	$\lvert\bar{i}_g^h\rvert$ (A)		$\lvert\bar{v}_{c,ll}^h\rvert$ (V)	
	Theory	Experimental	Theory	Experimental
S–VSC	1.93	1.86	26.57	26
VISMA II	1.4	1.17	27	27
KHI	14.18	15.32	39.3	39.7
Osaka	4.48	4.15	24.43	24
Osaka II	7.74	7.53	21.75	21.3
VISMA	0.49	0.32	27.95	28
VSYNC	4.85	4.92	32.23	33.3

TABLE IV: Results of Test 2: Inverse Sequence.

Model	$\lvert\bar{i}_g^h\rvert$ (A)		VUF (%)	
	Theory	Experimental	Theory	Experimental
S–VSC	9.53	9.22	4.69	4.51
VISMA II	6.85	6.58	4.77	4.61
KHI	10.7	10.99	5.27	5.42
Osaka	20.44	20.09	4.25	4.2
Osaka II	15.95	16.05	5.22	5.36
VISMA	3.59	3.58	4.91	4.9
VSYNC	5.04	5.11	5.13	5.22

VSC, VISMA II and Osaka models actuate a positive behavior by reducing the unbalance, as it can be noted in Fig. 8a, Fig. 8b and Fig. 8d, respectively. Indeed, the RMS voltage of the smallest phase (C2) increases with respect to the initial condition (M2), whereas the other two phases show a decrease, leading to a reduction of the VUF. On the contrary, the KHI (Fig. 8c), the Osaka II (Fig. 8e) and the VSYNC (Fig. 8g) models amplify the unbalance: phase b becomes much smaller (C2 against M2) and phase c increases (C3 against M3), leading to a VUF higher than 5%. In this case, indeed, neither the configuration C nor the configuration E satisfies (22). Finally, the VISMA model slightly reduces the unbalance of the PCC voltage by injecting a non–negligible current, as it can be observed in Fig. 8f.

TABLE V: Harmonic and unbalance sink capability of the VSMs under study.

Group	Model	Harmonic and Unbalance Sink Capability			
		Tunable	Harmonic	Inverse Sequence	Z_v Restrain
A	S–VSC	✔	✔	✔	✔
B	VISMA II	✔	✔	✔	✔
C	KHI	✔	✘	✘	✘
D	Osaka	✘	✔	✔	–
E	Osaka II	✔	✔	✘	✘
F	VISMA	✘	✔	✔	–
	VSYNC	✘	✘	✘	–

V. Conclusion

Virtual Synchronous Machines represent a promising solution to make renewable energy plants able to provide grid services, such as harmonic and unbalance sink capability.

This paper proposed a general method to foresee the response of different VSM configurations. The proposed method has been experimentally validated on five VSM models belonging to different configurations. The theoretical analysis, supported by experimental results, demonstrated the validity and reliability of the simplified modeling approach. Indeed, it can identify which VSM configuration can feature a beneficial harmonic and unbalance compensation by improving the voltage quality at the point of common coupling (PCC).

If (22) is fulfilled, the VSMs compensate the distortions. That is valid for VSM models with complete implementation of the virtual impedance (i.e., configurations A and B) and voltage source VSMs with no implementation of virtual impedance (i.e., configuration D), while the VSMs with a simplified impedance (i.e., configurations C and E) depend on the parameter selection.

As summarized in Table V, the VSM models with a complete implementation of the virtual impedance (e.g., S–VSC and VISMA II) can behave as harmonic and unbalance sinks, in compliance with the results of the simplified modeling. These models work as active filters, by improving the voltage quality at the PCC. Even the voltage source VSMs with no virtual impedance (e.g., Osaka) can provide a beneficial effect on the PCC voltage. However, their filtering capability is not tunable, as it depends on the physical parameters of the system (i.e., filter and grid impedances). Therefore, configurations A, B and D embed the needed features to make VSMs able to work as harmonic and unbalance sink with no constrains in the virtual parameters choice. On the opposite, VSMs with a simplified implementation of the virtual impedance (e.g., KHI and Osaka II) can either amplify or reduce the voltage distortions at the PCC, according to the parameter selection. As configuration C does not fulfill (22), it amplifies the distortions at the PCC, while configuration E reduces the harmonic distortion but increases the unbalance of the PCC voltage as it satisfies (22) only for the fifth harmonic distortion. Finally, VSMs based on the PLL structure (e.g., VSYNC model) amplify the distortion and the unbalance of the PCC voltage.

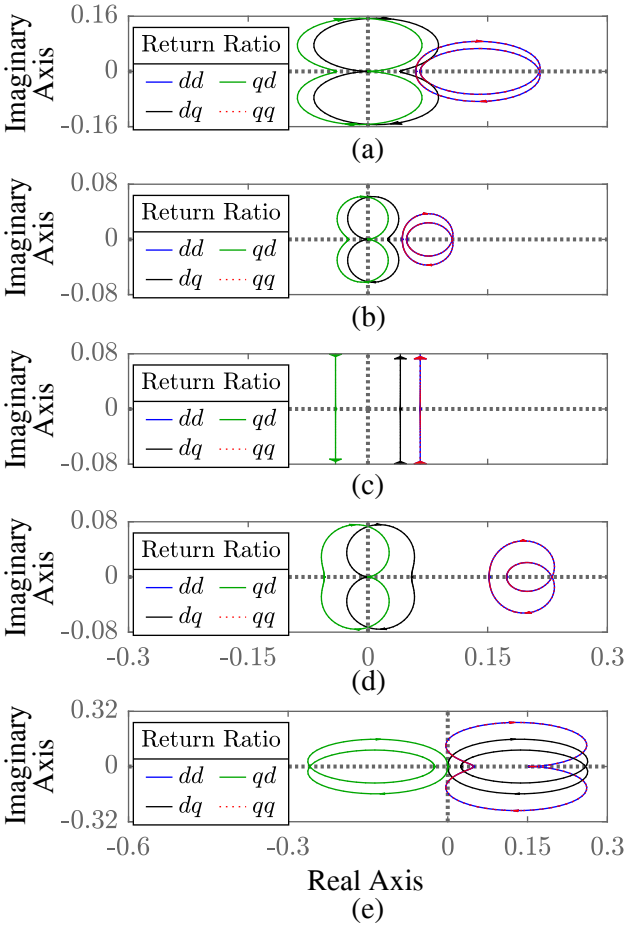

Fig. 9: Nyquist diagram of the return ratio $\mathbf{L}(\mathbf{s})$ for configuration: (a) A; (b) B; (c) C; (d) D; (e) E.

Appendix A

The stability of the virtual impedance implementation for the configurations A, B, C, D and E is evaluated according to the impedance–based stability criterion. By applying the Generalized Nyquist Criterion (GNC) on the return ratio it is possible to assess the stability of each configuration [39]. In the Laplace domain, in the (d, q) reference frame rotating at ω, the return ratio $\mathbf{L}(\mathbf{s})$ is defined as follows:

$$\mathbf{L}(\mathbf{s}) = \mathbf{Z_g}(\mathbf{s})\mathbf{Z_{out}^{-1}}(\mathbf{s}) \tag{25}$$

where $\mathbf{Z_g}(\mathbf{s})$ is the grid impedance matrix and $\mathbf{Z_{out}}(\mathbf{s})$ is the output impedance matrix of the converter.

$\mathbf{Z_g}(\mathbf{s})$ is the same for each configuration:

$$\mathbf{Z_g}(\mathbf{s}) = \begin{bmatrix} R_g + sL_g & -\omega L_g \\ \omega L_g & R_g + sL_g \end{bmatrix} \tag{26}$$

The $\mathbf{Z_{out}}(\mathbf{s})$ matrixes of each configuration can be retrieved from the equivalent circuits in Fig. 3:

$$\mathbf{Z_{out}^A}(\mathbf{s}) = \begin{bmatrix} R_v + sL_v & -\omega L_v \\ \omega L_v & R_v + sL_v \end{bmatrix} \tag{27}$$

$$\mathbf{Z_{out}^B}(\mathbf{s}) = \begin{bmatrix} (R_v + R_f) + s(L_v + L_f) & -\omega(L_v + L_f) \\ \omega(L_v + L_f) & (R_v + R_f) + s(L_v + L_f) \end{bmatrix} \tag{28}$$

$$\mathbf{Z_{out}^{C}} = \begin{bmatrix} R_v & -\omega L_v \\ \omega L_v & R_v \end{bmatrix} \tag{29}$$

$$\mathbf{Z_{out}^{D}}(\mathbf{s}) = \begin{bmatrix} R_f + sL_f & -\omega L_f \\ \omega L_f & R_f + sL_f \end{bmatrix} \tag{30}$$

$$\mathbf{Z_{out}^{E}}(\mathbf{s}) = \begin{bmatrix} R_f + sL_f & -\omega (L_v + L_f) \\ \omega (L_v + L_f) & R_f + sL_f \end{bmatrix} \tag{31}$$

Finally, the return ratio of each configuration is a 2x2 matrix, defined as follows:

$$\mathbf{L}(\mathbf{s}) = \begin{bmatrix} L_{dd}(s) & L_{dq}(s) \\ L_{qd}(s) & L_{qq}(s) \end{bmatrix} \tag{32}$$

By applying the GNC on the return ratio of each configuration it is possible to assess their stability. The results are shown in Fig. 9. As it can be observed, in each case the Nyquist diagram does not encircle the point (-1, $j0$). Therefore, all the configurations are stable [40].

REFERENCES

[1] VDE, "VDE-AR-n 4110 - Connection and Operation to Medium-Voltage Grid, 2018."

[2] U. Tamrakar, D. Shrestha, M. Maharjan, B. P. Bhattarai, T. M. Hansen, and R. Tonkoski, "Virtual Inertia: Current Trends and Future Directions," *Applied Sciences*, vol. 7, no. 7, p. 654, Jul. 2017.

[3] M. Chen, D. Zhou, and F. Blaabjerg, "Modelling, Implementation, and Assessment of Virtual Synchronous Generator in Power Systems," *Journal of Modern Power Systems and Clean Energy*, vol. 8, no. 3, pp. 399–411, May. 2020.

[4] V. Mallemaci, F. Mandrile, S. Rubino, A. Mazza, E. Carpaneto, and R. Bojoi, "A comprehensive comparison of Virtual Synchronous Generators with focus on virtual inertia and frequency regulation," *Electric Power Systems Research*, vol. 201, p. 107516, Dec. 2021.

[5] ENTSO-E, "High Penetration of Power Electronic Interfaced Power Sources and the Potential Contribution of Grid Forming Converters," Jan. 2020, technical Report.

[6] A. Tarrasó, J. I. Candela, J. Rocabert, and P. Rodriguez, "Grid voltage harmonic damping method for spc based power converters with multiple virtual admittance control," in *2017 IEEE Energy Conversion Congress and Exposition (ECCE)*, pp. 64–68, 2017.

[7] L. Zhou, Z. Shuai, Y. Chen, W. Wu, X. Zhou, K. Yan, and A. Luo, "Impedance-Based Harmonic Current Suppression Method for VSG Connected to Distorted Grid," *IEEE Transactions on Industrial Electronics*, vol. 67, no. 7, pp. 5490–5502, Jul. 2020.

[8] E. Avdiaj, J. Are Suul, S. D'Arco, and L. Piegari, "A Current Controlled Virtual Synchronous Machine Adapted for Operation under Unbalanced Conditions," in *2020 9th International Conference on Renewable Energy Research and Application (ICRERA)*, pp. 263–270, Sep. 2020, iSSN: 2572-6013.

[9] G. Lou, Q. Yang, W. Gu, X. Quan, J. M. Guerrero, and S. Li, "Analysis and Design of Hybrid Harmonic Suppression Scheme for VSG Considering Nonlinear Loads and Distorted Grid," *IEEE Transactions on Energy Conversion*, vol. 36, no. 4, pp. 3096–3107, Dec. 2021.

[10] T. S. Amorim, D. Carletti, and L. F. Encarnação, "Comparison of inverter controllers with synthetic inertia and harmonic compensation features," *Electric Power Systems Research*, vol. 197, p. 107344, Aug. 2021.

[11] F. Mandrile, E. Carpaneto, and R. Bojoi, "Grid-Feeding Inverter With Simplified Virtual Synchronous Compensator Providing Grid Services and Grid Support," *IEEE Transactions on Industry Applications*, vol. 57, no. 1, pp. 559–569, Jan. 2021.

[12] Y. P. Chen, R. Hesse, D. Turschner, and H.-P. Beck, "Comparison of methods for implementing virtual synchronous machine on inverters," *Renewable energy & power quality journal*, pp. 734–739, 2012.

[13] K. Sakimoto, Y. Miura, and T. Ise, "Stabilization of a power system with a distributed generator by a virtual synchronous generator function," in *8th International Conference on Power Electronics - ECCE Asia*, pp. 1498–1505, 2011.

[14] Jia Liu, Y. Miura, and T. Ise, "Dynamic characteristics and stability comparisons between virtual synchronous generator and droop control in inverter-based distributed generators," in *2014 International Power Electronics Conference (IPEC-Hiroshima 2014 - ECCE ASIA)*, pp. 1536–1543, 2014.

[15] J. Liu, Y. Miura, H. Bevrani, and T. Ise, "Enhanced virtual synchronous generator control for parallel inverters in microgrids," *IEEE Transactions on Smart Grid*, vol. 8, no. 5, pp. 2268–2277, 2017.

[16] Y. Hirase, K. Abe, K. Sugimoto, and Y. Shindo, "A grid connected inverter with virtual synchronous generator model of algebraic type," *IEEJ Transactions on Power and Energy*, vol. 132, pp. 371–380, 01 2012.

[17] Y. Hirase, K. Sugimoto, K. Sakimoto, and T. Ise, "Analysis of resonance in microgrids and effects of system frequency stabilization using a virtual synchronous generator," *IEEE Journal of Emerging and Selected Topics in Power Electronics*, vol. 4, no. 4, pp. 1287–1298, 2016.

[18] H. Beck and R. Hesse, "Virtual synchronous machine," in *2007 9th International Conference on Electrical Power Quality and Utilisation*, pp. 1–6, 2007.

[19] R. Hesse, D. Turschner, and H.-P. Beck, "Micro grid stabilization using the virtual synchronous machine, (VISMA)," *Renewable energy & power quality journal*, vol. 1, pp. 676–681, 2009.

[20] M. P. N. van Wesenbeeck, S. W. H. de Haan, P. Varela, and K. Visscher, "Grid tied converter with virtual kinetic storage," in *2009 IEEE Bucharest PowerTech*, pp. 1–7, 2009.

[21] Y. Chen, R. Hesse, D. Turschner, and H.-P. Beck, "Dynamic properties of the virtual synchronous machine (VISMA)," *Renewable energy & power quality journal*, pp. 755–759, 2011.

[22] M. Blau and G. Weiss, "Synchronverters used for damping inter-area oscillations in two-area power systems," *Renewable Energy and Power Quality Journal*, pp. 45–50, 04 2018.

[23] P. Rodriguez, I. Candela, and A. Luna, "Control of pv generation systems using the synchronous power controller," in *2013 IEEE Energy Conversion Congress and Exposition*, pp. 993–998, 2013.

[24] W. Zhang, A. Luna, I. Candela, J. Rocabert, and P. Rodriguez, "An active power synchronizing controller for grid-connected power converters with configurable natural droop characteristics," in *2015 IEEE 6th International Symposium on Power Electronics for Distributed Generation Systems (PEDG)*, pp. 1–7, 2015.

[25] N. B. Lai, G. N. Baltas, and P. Rodriguez, "Multi-Rotor Virtual Machine for Grid-Forming Converter to Damp Sub-Synchronous Resonances," *IEEE Access*, vol. 9, pp. 128 178–128 187, 2021.

[26] V. Natarajan and G. Weiss, "Synchronverters With Better Stability Due to Virtual Inductors, Virtual Capacitors, and Anti-Windup," *IEEE Transactions on Industrial Electronics*, vol. 64, no. 7, pp. 5994–6004, Jul. 2017.

[27] X. Liang, C. Andalib-Bin-Karim, W. Li, M. Mitolo, and M. N. S. K. Shabbir, "Adaptive Virtual Impedance-Based Reactive Power Sharing in Virtual Synchronous Generator Controlled Microgrids," *IEEE Transactions on Industry Applications*, vol. 57, no. 1, pp. 46–60, Jan. 2021.

[28] M. Ren, T. Li, K. Shi, P. Xu, and Y. Sun, "Coordinated Control Strategy of Virtual Synchronous Generator Based on Adaptive Moment of Inertia and Virtual Impedance," *IEEE Journal on Emerging and Selected Topics in Circuits and Systems*, vol. 11, no. 1, pp. 99–110, Mar. 2021.

[29] J. Guo, Y. Chen, S. Liao, W. Wu, L. Zhou, Z. Xie, and X. Wang, "Analysis and Mitigation of Low-Frequency Interactions Between the Source and Load Virtual Synchronous Machine in an Islanded Microgrid," *IEEE Transactions on Industrial Electronics*, vol. 69, no. 4, pp. 3732–3742, Apr. 2022.

[30] S. D'Arco, J. A. Suul, and O. B. Fosso, "Control system tuning and stability analysis of virtual synchronous machines," in *2013 IEEE Energy Conversion Congress and Exposition*, pp. 2664–2671, 2013.

[31] S. D'Arco, J. A. Suul, and O. B. Fosso, "Small-signal modeling and parametric sensitivity of a virtual synchronous machine in islanded operation," *International Journal of Electrical Power & Energy Systems*, vol. 72, pp. 3 – 15, 2015.

[32] A. Rodriguez-Cabero, J. Roldan-Perez, and M. Prodanovic, "Virtual Impedance Design Considerations for Virtual Synchronous Machines in Weak Grids," *IEEE Journal of Emerging and Selected Topics in Power Electronics*, vol. 8, no. 2, pp. 1477–1489, Jun. 2020.

[33] H. Wu and X. Wang, "Small-Signal Modeling and Controller Parameters Tuning of Grid-Forming VSCs With Adaptive Virtual Impedance-Based Current Limitation," *IEEE Transactions on Power Electronics*, vol. 37, no. 6, pp. 7185–7199, Jun. 2022.

[34] X. Quan, A. Q. Huang, and H. Yu, "A Novel Order Reduced Synchronous Power Control for Grid-Forming Inverters," *IEEE Transactions on Industrial Electronics*, vol. 67, no. 12, pp. 10 989–10 995, Dec. 2020.

[35] C. Li, Y. Yang, N. Mijatovic, and T. Dragicevic, "Frequency Stability Assessment of Grid-Forming VSG in Framework of MPME With Feedforward Decoupling Control Strategy," *IEEE Transactions on Industrial Electronics*, vol. 69, no. 7, pp. 6903–6913, Jul. 2022.

[36] J. Grainger and W. Stevenson, *Power System Analysis*. McGraw Hill, 1994.
[37] N. Tleis, *Power Systems Modelling and Fault Analysis*. Elsevier, 2019.
[38] P. Rodriguez, A. Luna, I. Candela, R. Mujal, R. Teodorescu, and F. Blaabjerg, "Multiresonant Frequency-Locked Loop for Grid Synchronization of Power Converters Under Distorted Grid Conditions," *IEEE Transactions on Industrial Electronics*, vol. 58, no. 1, pp. 127–138, Jan. 2011.
[39] J. Sun, "Impedance-based stability criterion for grid-connected inverters," *IEEE Transactions on Power Electronics*, vol. 26, no. 11, pp. 3075–3078, 2011.
[40] J. M. Maciejowski, *Multivariable feedback design*. Addison-Wesley, 1989.

Vincenzo Mallemaci (S'20) was born in Messina, Italy, in 1996. He received the Bachelor and Master degrees both in electrical engineering from Politecnico di Torino, Italy, in 2018 and 2020, respectively. He is currently a Ph.D. student at Dipartimento Energia "G. Ferraris" at Politecnico di Torino. His Ph.D. activity focuses on virtual synchronous machines and control for power electronic grid–connected converters.

Fabio Mandrile (S'18, M'21) received the M.Sc. and Ph.D. degrees in electrical engineering from Politecnico di Torino, Italy, in 2017 and 2021, respectively. He is currently assistant professor at Dipartimento Energia "G. Ferraris" at Politecnico di Torino. His main research interests are virtual synchronous machines and power electronics for grid-connected applications, on which he focused his Ph.D. and current research activity.

Enrico Carpaneto (M'86) was born in Torino, Italy, in 1959. He received the M.Sc. and Ph.D. degrees in electrical engineering from Politecnico di Torino, Torino, Italy, in 1984 and 1989, respectively. He is currently an Associate with the Energy Department, Politecnico di Torino. His research activities cover many different aspects of modeling, simulation and optimization of generation, transmission and distribution systems. He has published more than 100 scientific papers. He has been responsible for several research contracts concerning analysis, operation and planning of distribution networks, power quality, and generation optimization. His current research interests include distribution systems, dispersed generation, virtual synchronous generators, and thermal models. Dr. Carpaneto is a member of the IEEE Power Engineering Society and Associazione Italiana di Elettrotecnica, Elettronica, Automazione, Informatica e Telecomunicazioni (AEIT).

Radu Bojoi (SM'10, F'19) received the M.Sc. degree from Technical University of Iasi, Romania, in 1993, and the Ph.D. degree from Politecnico di Torino, Torino, Italy, in 2002, all in electrical engineering. He is a Full Professor of Power Electronics and Electrical Drives with the Energy Department G. Ferraris and Chairman of the Power Electronics Innovation Center, Politecnico di Torino. He has authored or coauthored more than 150 papers covering electrical drives and power electronics for industrial applications, transportation electrification, power quality, and home appliances. He was involved in many research projects with industry for direct technology transfer aiming at obtaining new products. Prof. Bojoi is the co-recipient of five prize paper awards, the last one in 2015 as IEEE-IAS Prize Paper Award. Dr. Bojoi is a Co-Editor-In-Chief of the IEEE Transactions on Industrial Electronics.